

Experimental Demonstration of Multiple Monoenergetic Gamma Radiography for Effective Atomic Number Identification in Cargo Inspection

Brian S. Henderson,^{a)} Hin Y. Lee, Thomas D. MacDonald, Roberts G. Nelson, and Areg Danagoulian
Department of Nuclear Science and Engineering, Massachusetts Institute of Technology, Cambridge, Massachusetts 02139

(Dated: 21 March 2018)

The smuggling of special nuclear materials (SNM) through international borders could enable nuclear terrorism and constitutes a significant threat to global security. This paper presents the experimental demonstration of a novel radiographic technique for quantitatively reconstructing the density and type of material present in commercial cargo containers, as a means of detecting such threats. Unlike traditional techniques which use sources of bremsstrahlung photons with a continuous distribution of energies, multiple monoenergetic gamma radiography (MMGR) utilizes monoenergetic photons from nuclear reactions, specifically the 4.4 and 15.1 MeV photons from the $^{11}\text{B}(\text{d},\text{n}\gamma)^{12}\text{C}$ reaction. By exploiting the Z -dependence of the photon interaction cross sections at these two specific energies it is possible to simultaneously determine the areal density and the effective atomic number as a function of location for a 2D projection of a scanned object. The additional information gleaned from using and detecting photons of specific energies for radiography substantially increases the resolving power between different materials. This paper presents results from the imaging of mock cargo materials ranging from $Z \approx 5$ –92, demonstrating accurate reconstruction of the effective atomic number and areal density of the materials over the full range. In particular, the system is capable of distinguishing pure materials with $Z \gtrsim 70$, such as lead and uranium — a critical requirement of a system designed to detect SNM. This methodology could be used to screen commercial cargoes with high material specificity, to distinguish most benign materials from SNM, such as uranium and plutonium.

I. INTRODUCTION

The field of nuclear security addresses the danger of the nuclear weapons, including proliferation of weapon technology, safeguards of fissile materials, and the risk of nuclear terrorism. The latter topic encompasses cargo security, which specifically focuses on preventing the smuggling of nuclear materials and fully assembled nuclear devices through ports of entry and other pathways. Estimates of the immediate economic costs alone of a nuclear explosion in a major port exceed \$1 trillion, *before* accounting for the substantial human costs^{1,2}. Given the relative anonymity of cargo shipping and its resulting vulnerability to smuggling, the lack of systems to efficiently and reliably deter nuclear smuggling remains a relevant security threat. This paper details the demonstration of a new radiography technique for quantitatively identifying materials in cargo that is capable of distinguishing different materials with high atomic number. Specifically, the technique is capable of separating benign high- Z materials such as lead and tungsten from special nuclear materials (SNM).

A. Detecting Nuclear Material in Cargo

Approximately 40000–57000 maritime shipping containers enter the United States every day³. This fast throughput rate and the fact that many containers are

densely packed to weights of up to 20 metric tons make cargo containers particularly vulnerable to the smuggling of nuclear materials or weapons. A system designed to detect nuclear smuggling must simultaneously achieve the following: scan cargo at $\lesssim 1$ minute per container, produce a low rate of false positives, and provide a clear indicator of the presence of nuclear materials in diverse cargo configurations (i.e., a low rate of false negatives). Additionally, port operations restrict the footprint of scanning systems, as well as the permissible radiation dose to the cargo and surrounding area^{4,5}.

Cargo screening technologies can be classified into three categories: passive interrogation, active interrogation, and radiography. Passive interrogation involves the detection of the natural radioactivity of various particles — neutrons and photons in particular — from fissile materials. In this context the materials of interest are primarily weapons grade uranium (WGU), which consists primarily of ^{235}U , and weapons grade plutonium (WGPu). The later primarily consists of ^{239}Pu , but its other isotopes (^{240}Pu in particular) play a key role in its passive signature.

Passive detection systems offer simplicity and relatively low cost, and such systems have been deployed widely in the United States and elsewhere. These systems primarily consist of portals, which use various scintillators to detect photons in combination with ^3He neutron detectors to uncover SNM by their radioactive emissions from nuclear decay and spontaneous fission. The addition of shielding around smuggled material, however, circumvents passive detection. The passive signal from WGU is very weak and easily shielded, while even an assembled plutonium device (with its strong spontaneous

^{a)}E-Mail: bhender1@mit.edu

fission neutron signature) may be shielded with combinations of low- and high- Z material to block both neutron and photon signals.

The limitations of passive detection techniques necessitate alternative approaches. Active interrogation systems expose the cargo to a beam of one or more types of particles (such as photons, neutrons, or muons) to trigger secondary processes unique to fissionable and fissile materials, producing signals which are strong enough to overcome shielding attempts by a competent smuggler. Examples of such systems include prompt neutrons from photofission (PNPF)⁶, EZ3D⁷, and nuclear resonance fluorescence⁸. Furthermore, other groups related to this research effort have advanced the detection of delayed neutrons from induced fission as a way of identifying fissile materials⁹. While such techniques have promise due to their specificity for SNM detection, no system has been sufficiently developed for deployment at this time. For a high level discussion of several active detection methodologies see Runkle, *et al.*¹⁰.

B. Radiography for SNM Detection

While searching for shielded fissile and fissionable materials via active methods is promising, shielding scenarios which completely block the signal are nevertheless possible. Radiographic imaging of cargo provides a means of detecting such scenarios. A variety of radiographic techniques have been proposed in the past, including using medium energy (\sim GeV) protons¹¹, muons^{12–14}, neutrons^{15–17}, as well as \sim keV photons (X-rays) and \sim MeV photons (gamma rays)^{18,19}. Additionally, radiographic imaging of cargo for SNM overlaps well with other goals of cargo inspection (such as detection of non-nuclear smuggling), adding value to the technique.

This work builds upon prior studies of using 4.4 and 15.1 MeV monochromatic photons from the $^{11}\text{B}(d, n\gamma)^{12}\text{C}$ reaction to radiograph objects and differentiate between their material types^{20,21}. A parallel effort by other groups, using Cherenkov detectors, have used the same reaction to pursue a similar goal²². The prior work however did not achieve a precise determination of the atomic number or areal density of the scanned objects. This work demonstrates the ability to infer the effective atomic number (Z) and areal density (ρ_A) of a given spatial pixel across a cargo sample, providing essential information for the identification of materials present in the cargo. This reconstruction is shown to be accurate enough to distinguish between uranium and lead, a critical result for SNM detection in that it permits distinguishing nuclear threats from benign materials. With this capability, the system is robust against false alarm scenarios in which benign high- Z materials (e.g., lead, tungsten, precious metals) appear similar to SNM and thus require further inspection.

In its simplest form radiography combines measurements the transmitted photon flux ϕ for a given mate-

rial sample, knowledge of the incident flux ϕ_0 , and an assumption of the mass attenuation coefficient μ of the material to infer an approximate areal density ρ_A :

$$\mu\rho_A = \ln(\phi_0/\phi) . \quad (1)$$

This calculation can be performed for every pixel in a radiographic scan to image the sample. By assuming that μ does not vary through the scan plane, a *relative* value of ρ_A can be reconstructed. It should be noted that μ depends on the elemental composition of the material, and thus is a function of effective atomic number Z . As such, a measurement such as this cannot allow a simultaneous determination of effective atomic number Z and areal density ρ_A , a requirement for distinguishing SNM from benign cargo.

This goal can be achieved by using the energy dependence of μ , and performing multiple measurements at various energies. The main processes which contribute to photon attenuation at 4.4 and 15.1 MeV are Compton scattering and pair production. The mass attenuation coefficient can be approximated as $\mu = \mu_c + \mu_{pp}$, where μ_c and μ_{pp} are the coefficients for Compton scattering and pair production, respectively. Each of these coefficients depends on Z and the incident photon energy E in different ways. Specifically,

$$\begin{aligned} \mu_c &= ZN_A\sigma_c(E, Z)/A \\ \mu_{pp} &= N_A\sigma_{pp}(E, Z)/A, \end{aligned}$$

where N_A is Avogadro's number, A is the atomic weight of the material under inspection, and the $\sigma(E, Z)$ are the cross sections of the relevant attenuation processes. For photon energies satisfying $E \gg 511$ keV, the cross sections may be approximated as $\sigma_c \propto 1/E$ and $\sigma_{pp} \propto Z^2 f(E_\gamma)$, where $f(E_\gamma)$ is a function of energy with negligible dependence on atomic number²³. Using these as inputs to the mass attenuation coefficients to compute the transmission ratios (Equation 1) at two different energies (E_0 and E_1) results in

$$\begin{aligned} R &= \frac{\ln(\phi(E_1)/\phi_0(E_1))}{\ln(\phi(E_0)/\phi_0(E_0))} = \frac{Z^2 f(E_1)N_A \cdot \text{const}_1/A}{ZN_A \cdot \text{const}_2/AE_0} \\ &= Z \cdot E_0 f(E_1)C, \end{aligned} \quad (2)$$

where C is a constant equal to the ratio $\text{const}_1/\text{const}_2$. This treatment assumes that at E_0 the mass attenuation is entirely dominated by Compton scattering, while at E_1 pair production dominates. Assuming these requirements are met, an experimental measurement of R could be used to directly determine the atomic number Z (and the total attenuation used to infer the areal density ρ_A). While this simple model requires broad approximations, Equation 2 captures the essential mechanism by which dual energy radiography may provide precise identification of the effective Z of inspected materials.

C. Monoenergetic Gamma Rays from Nuclear Reactions

Dual energy radiography is by no means a new concept. Current systems implement this technique by using bremsstrahlung beams with varying endpoints. Linear accelerator (linac) based bremsstrahlung dual energy systems typically vary the electron beam energy between two fixed values (e.g., 6 and 9 MeV)^{18,19}. The transmitted signals are compared in a way that allows quantitative determination of the effective Z of a given pixel in the cargo image²⁴. Bremsstrahlung based systems, while capable of rapidly producing images with excellent spatial resolution using commercially-produced equipment, have notable disadvantages. Most commercial linacs produce have a duty factor of $\sim 0.1\%$, producing pulses of several μs length at $\mathcal{O}(10^2 \text{ Hz})$. The resulting large instantaneous flux prevents measurement of the transmitted spectrum and only an integrated measurement of the total deposited energy is possible. This significantly reduces the information content of the signal, increasing the number of photons (and thus radiation dose) required to reconstruct the material type. Furthermore, most of the energy of the beam flux is at low energies ($\lesssim 1 \text{ MeV}$). Photons at these energies contribute to radiation dose, but provide little to no transmitted information due to the strong attenuation at low energies. For example, a Geant4²⁵ simulation shows that a system based on a 6 MeV electron beam would produce approximately 90% of the counts and 65% of the radiation dose from photons $\leq 3 \text{ MeV}$. This translates to a low information-to-dose ratio. Finally, a significant number of photons undergo scattering in the cargo but still reach the detectors, which reduces the image contrast and dilutes the pixel-specific Z -dependent information content.

Many of these factors can be overcome by replacing a linac-based system with one which uses nuclear reactions to produce monochromatic photons. The technique of using monoenergetic gamma rays at several energies, referred to as multiple monoenergetic gamma radiography (MMGR), provides several advantages over traditional bremsstrahlung radiography. The knowledge of the photon energies and the measurement of transmitted spectral data allows the suppression of events in the signal which have undergone scattering, thus leaving only the photons which have undergone direct line-of-sight transmission. This creates a clean transmitted signal associated with each pixel, highly dependent on the effective Z and areal density of the intervening material. This work utilizes the $^{11}\text{B}(d,n\gamma)^{12}\text{C}$ reaction to produce 4.4 and 15.1 MeV photons, which arise from the short-lived excited levels of ^{12}C in the final state of the reaction. The large spread in energy between the two gamma rays in the source spectrum provide strong leverage for material identification.

II. EXPERIMENTAL METHODS

To test the capability of the MMGR technique, a mock cargo scanning setup was constructed at the MIT-Bates Research and Engineering Center, a schematic of which is shown in Figure 1. This setup expanded upon previous test experiments^{15,21} to permit the 2D imaging of mock cargo materials. This included the installation of a motion system to move mock cargo materials through the beam, an array of 32 detectors to provide position resolution perpendicular to the direction of the motion, and the addition of a number of beam and data diagnostics to monitor the system over the course of a scan. This section describes the key elements of the experiment and mock cargo scenario for which data was collected.

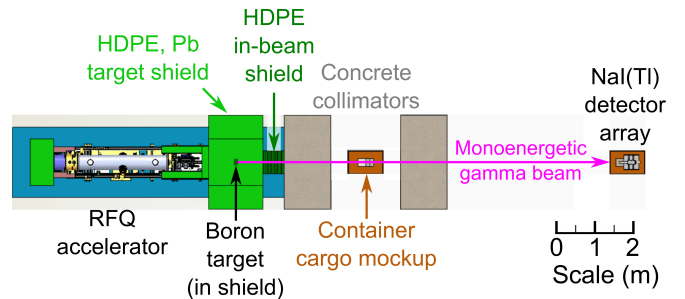


FIG. 1. Schematic of the mock cargo scanning experiment, viewed from above²¹. The arrow associated with the mock cargo label indicates the direction of motion of the cargo across the scan.

A. Gamma Ray Beam

The 4.4 and 15.1 MeV photons used to radiograph materials were generated by impinging a 3 MeV deuteron (d^+) beam on a thick natural boron target, containing 80.1% ^{11}B . Given the relative cross sections of the $^{11}\text{B}(d,n\gamma)^{12}\text{C}$ for the 4.4 and 15.1 MeV gammas at this energy, the beam on target produced the two gammas in approximately a 4:1 ratio^{26,27}. The deuterons were accelerated using an Accsys Technologies DL-3 Radio Frequency Quadrupole (RFQ) accelerator, and the target was mounted to the output port of the RFQ. The accelerator operated at a frequency of 300 Hz, producing deuteron beam pulses of approximately 20 μs (0.6% duty factor) as shown in Figure 3. Thus, while the time average deuteron current during experiments was approximately 10 μA , the instantaneous current during the beam pulses reached $\sim 1.7 \text{ mA}$.

The reactions at the target generated gamma rays approximately isotropically²⁷. Thus, high-density concrete collimators were used to create a fan beam extending vertically with an illumination width of 2.38 cm in the horizontal direction at the location of the mock cargo. Additionally, 53 cm of borated high density polyethylene (HDPE) was placed directly downstream of the target

(encompassing the entire fan beam) to block neutrons and low energy photons from secondary reactions in the target. Figure 2 shows the spectrum of the beam measured at low event rate to show the key features, including the 4.4 MeV and 15.1 MeV gammas. An additional contribution is visible at 1.7 MeV (from $^{11}\text{B}(\text{d},\text{p}\gamma)^{12}\text{B}$ and peaks between 6 and 9 MeV result from thermal neutron capture in the detectors and surrounding materials. See O'Day, *et al.*²¹ for an extended discussion of the beam components.

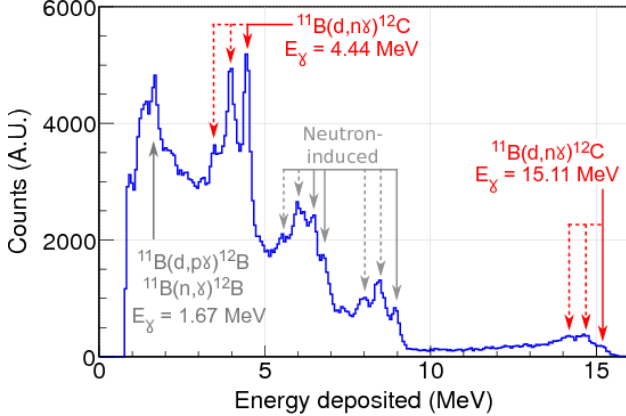


FIG. 2. Sample spectrum measured in the NaI (Tl) detectors with an iron sample in the beam and $\sim 1 \mu\text{A}$ deuteron current, so as to show the features with high resolution. See O'Day, *et al.*²¹ for a discussion of the labeled elements of the spectrum.

B. Detectors

The transmitted spectra were measured using a vertical array of 32 Saint-Gobain 2X4H16/2SS NaI(Tl) scintillator detector packages²⁸. The detectors consisted of $2'' \times 4'' \times 16''$ thallium-doped sodium iodide crystals instrumented with $2''$ photomultiplier tubes. The large size and appreciable energy resolution of these detectors allowed the selection of directly transmitted monoenergetic photons, providing critical information for precision material identification. The high voltage and gain controls were manually adjusted for each detector to approximately match their responses, although further energy calibration (gain) corrections were applied in analysis (see Section III A 1). The array was constructed so that the long axis of the detectors was parallel to the beam axis and the short axis was along the vertical direction to maximize the vertical spatial resolution of the detector array. The detector array was placed such that the upstream faces of the detectors were 9.35 m from the boron target (or approximately 5.81 m from the mock cargo). This resulted in approximately 3 cm vertical resolution for the cargo imaging. The horizontal extent of the detectors perpendicular to the beam was wider than

the collimation, and thus did not significantly affect the imaging resolution.

C. Data Acquisition

The detector pulses were processed using CAEN V1725 digitizer modules operating in digital pulse processing pulse shape discrimination (DPP-PSD) mode²⁹. The system was configured such that the trigger threshold for each detector approximately corresponded to a 1 MeV energy deposition. The pulse integration window for each trigger was 1 μs . Note that unlike standard radiography systems, which operate in charge integrating mode, the system described here recorded individual waveforms with timing and pulse shape information available for each detection. This allowed the use of several analysis techniques described in Section III to increase the resolution of the system in effective Z and areal density. The digitizer output was processed using an extension to the ADAQ analysis framework to produce data files for analysis³⁰.

D. Mock Cargo Test Configuration

To utilize this system as a cargo scanning prototype, a motion system installed between the concrete collimators (as shown in Figure 1) moved materials samples placed on a cart (shown in Figure 9) across the fan beam over the course of an experimental run. Data were collected as a function of time, which, when paired with the known motion of the materials and the vertical resolution of the detector array, allowed the 2D imaging of the mock cargo materials. The materials tested were chosen so as to span a large range of effective Z (~ 5 –82) and to include a stand-in for SNM (natural uranium rods with aluminum cladding—see Appendix A). The areal densities of the materials were chosen so as to approximate typical total areal densities present in commercial cargo containers. Table I summarizes the parameters of the materials samples.

Section IV presents results from two distinct experimental runs using the same materials samples: one in which the cargo was moved across the beam at 0.0077 cm/s and one in which the cargo was moved at 0.308 (4x the speed of the first test). These are referred to as the 7400 s and 2000 s scans respectively. Additionally, the data could be sampled to considerably finer time resolution (4 ns), permitting the oversampling of the data relative to the collimator width to improve the horizontal position resolution of the reconstruction. Analyses were conducted using 1 cm and 1 mm pixel widths, as discussed in Sections III and IV. Note that while these scan times are considerably longer than would be feasible for a deployed cargo scanner, the relevant quantity is the integrated deuteron beam current delivered on target per unit scan distance, since scan times may be reduced

by increasing the beam current. In the 7400 s run, the beam charge delivered was 1.3 mC/cm of scan length (at 10 μ A of average beam current). This would correspond to scan times of ~ 100 s for full sized containers with 1 mA average beam current. Such currents would likely be achievable using a purpose-designed accelerator (operating with continuous wave current).

III. ANALYSIS

To reconstruct the effective Z and areal density of the mock cargo, the transmitted gamma ray spectra were compared to the expected spectra based on a detailed simulation model of the experiment. The data spectra were collected over fixed increments of the scan length for each detector channel to create “pixels” for the material reconstruction. Similarly to standard radiography techniques, the analysis consisted of comparing the transmitted spectra with materials in the beam to that of the “open” beam, i.e., when no materials were present in the beam other than the fixed components of the setup described in Section II. This comparison provides information of the total attenuation of the beam due to the material as well as the energy dependence of this attenuation, which provides sufficient information to reconstruct the total areal density and effective atomic number of the materials.

The simulation model was used to generate a library of materials over the complete space of $Z = 4\text{--}92$ and areal density $\rho_A = 20\text{--}250$ g/cm². The use of the simulation library allowed for the reconstruction of the cargo materials without empirical calibration based on additional datasets and provided a means of directly accounting for detector response and efficiency, collimation of the beam, multiple/down-scattering of transmitted photons, and other elements of the physical setup. This section describes the procedures applied to prepare the data spectra for comparison with the simulated transmission library, the simulation model, and the analysis used to extract the effective Z and areal density of the mock cargo.

A. Spectrum Corrections

Several corrections were applied to the raw spectra, both to ensure consistency across an imaging scan and to select the relevant data for comparison with the simulation model. Unlike traditional gamma/x-ray cargo radiography systems, which utilize integration mode detectors to cope with the high photon flux of bremsstrahlung beams³², the lower absolute photon flux of the nuclear reaction based photon beam here permits use of detectors in counting mode. This makes it possible to record the complete energy dependence of the transmitted spectra. This spectral information allows individual recorded events to be associated with the initial photon energy and thus more accurate determination of the attenuation of

the beam due to the cargo at the specific beam energies. To produce spectra representative of the transmission of the monoenergetic photons, several corrections must be applied to the raw spectra. The corrections are described as follows in the order they were applied to the raw data.

1. Gain Drift Correction

As the experiment operated in a non-climate controlled warehouse, the NaI (Tl) detectors were subject to gain drift on the order of several percent over the course of each scan. Since the analysis depends on the measurement of counts recorded in specific energy regions of the data spectra, a fixed calibration of ADC counts to deposited energy for a detector would cause systematic error for each energy bin. To prevent this, the raw spectrum of each detector at each position step in the scan was used to determine the ADC-to-energy calibration at that specific step using the monoenergetic peaks present in the spectra to produce energy spectra that could be compared on equal footing.

2. Beam Timing Cut

The pulsed nature of the deuteron beam provided a means of suppressing many of the background contributions to the raw detected spectra. Since the lifetimes of the excited states of ¹²C that gave rise to the 4.4 and 15.1 MeV photons in the target are $\mathcal{O}(10^{-13}$ s), events from the gamma rays of interest were recorded promptly in coincidence with beam pulses. Gating on the beam pulse timing allowed for suppression of background events due to longer-lived excited states and thermal neutrons. In particular, bremsstrahlung photons arising from the beta decay of ¹²B (produced by neutron capture on ¹¹B in the target) contributed significantly to the raw signal up to 6.9 MeV. Given that the beta decay of ¹²B has a lifetime of ~ 20 ms, however, $\sim 99.9\%$ of its contribution to the raw spectra may be eliminated by selecting only events in the beam pulse time windows.

Since no timing information was recorded for the beam pulses during data taking and the exact frequency of the accelerator deviated slightly from 300 Hz, the pulse frequency was reconstructed by computing the mean time of concentrations of events in the detectors over many pulses. A symmetric 20 μ s window around the reconstructed pulse center was selected for the timing cut, as shown in Figure 3. Figure 4 shows the spectrum of the open beam inside and outside the timing cut, showing that the inclusion of events outside the time cut would contribute $\sim 10\%$ error to the estimated counts in the 4.4 MeV region. Notably, the 4.4 MeV signal remains visible in the off-pulse spectrum. This is due to the fact that the beta decay of ¹²B frequently creates the ¹²C 4.4 MeV excited state^{33,34}. Additionally visible are small peaks

Material	Effective Z	Density (g/cm ³)	Width \times Height (cm \times cm)	Depth (cm)	Areal Density (ρ_A) (g/cm ²)
Borated HDPE	~ 5.2	1.02	20.3 \times 23.1	45.30	46.2
Aluminum (Al)	13	2.70	20.3 \times 24.5	20.25	54.7
Copper (Cu)	29	8.96	10.1 \times 10.1	5.45	48.8
Tin (Sn)	50	7.31	10.1 \times 10.1	6.74	49.3
Tungsten (W)	74	19.30	10.1 \times 10.1	2.56	49.4
Lead (Pb)	82	11.35	20.3 \times 20.3	5.08	57.7
Uranium rods	~ 65	12.72	13.8 \times 21.2	5.50	~ 55

TABLE I. Parameters of the materials samples used for the imaging test, the arrangement of which is shown in Figure 9. The effective Z value listed for the borated HDPE is computed as the average elemental composition of the material weighted by the contribution to the electron density by each element, since Compton scattering dominates the photon interactions at the energies of interest for the light nuclei comprising the material³¹. Values listed for the uranium rods are averaged over the arrangement of the 10 rods. See Appendix A for explanation of the effective Z and areal density for the uranium rods.

from the capture of thermal neutrons on hydrogen (2.2 MeV) and a longer lived excited state of ^{12}B (1.7 MeV)³⁵.

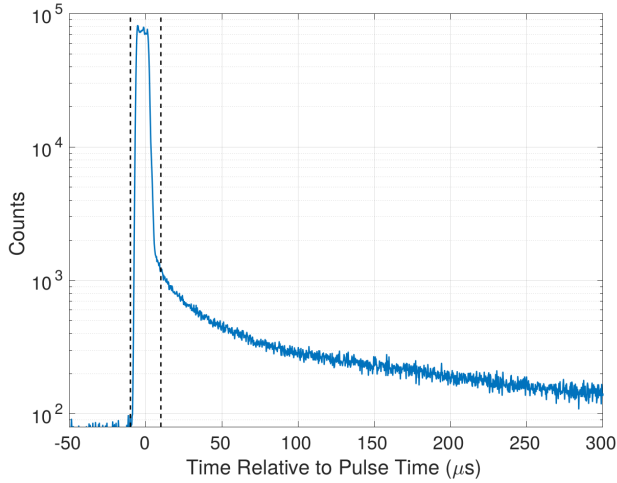


FIG. 3. Reconstructed beam pulse shape, time behavior of the after pulse events, and cut window applied to select only prompt events associated with beam pulses (dashed lines).

3. Beam Current Correction

Any unaccounted for variation in the deuteron current (and thus the beam flux) between the open beam and the subsequent measurements would caused an error in the transmission measurement directly proportional to the current variation. As noted in Section II, a charge integrator was used to monitor the beam current incident on the boron target over the course of each imaging scan. The beam current varied by up to $\sim 10\%$ during the imaging tests, primarily due to instabilities in the deuteron source and accelerator. The data from this channel were used to renormalize the data spectra at each position step. Note that only the relative beam current at each scan step is required, rather than an absolute calibration,

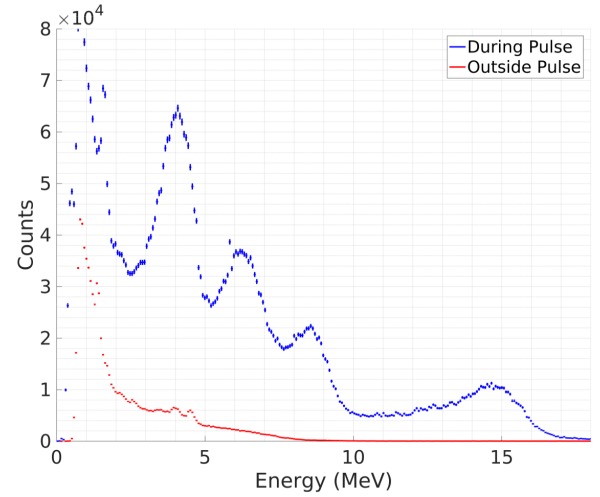


FIG. 4. Spectra of the open beam during and outside the beam pulse window (lower histogram, color online), with pile-up corrections applied (see Section III A 4). Events outside the pulses contributed approximately 13% of all raw counts, after correction for pile-up (Section III A 4).

since the analysis utilizes only the relative transmission between cargo-in-beam and the open beam. While an approximate calibration of the current was known, any uncertainty in its value does not significantly affect the reconstruction of the materials.

4. Pile-Up/Dead-Time Correction

The large size of the NaI (Tl) detectors in combination with the high instantaneous current of the pulsed RFQ beam resulted in a significant number of “pile-up” events in the raw spectra (i.e., single spectrum counts representing the energy deposition of two or more individual photons in the same pulse integration period). These pile-up events significantly distort the open beam spectrum. In particular, such events add an excess of events at higher

energies from the summation of two lower energy depositions. While standard radiography systems operating with integration mode detectors are not subject to this issue, the analysis described here — which utilizes spectral information — must carefully account for this effect.

A pulse shape discrimination (PSD) algorithm was used to identify such pile-up events in data. The “tail-over-total” PSD method, frequently used to separate gamma ray and neutron events in organic scintillators due to their differing scintillation decay time scales³⁶, may also be used to identify pile-up events. In this method, the charge integrated by the ADC for a PMT waveform is separated into “head” and “tail” portions at a fixed amount following the trigger. An energy deposition of any value resulting from a single event should exhibit roughly the same “tail-over-total” ratio, corresponding to the decay time of the scintillator. Integration windows with pile-up events will show an excess in the tail portion of pulse integration due to the contribution of the second pulse.

For the imaging scans, the pulse integration period was fixed at 1 μ s, and the tail region was defined to be approximately the last 50% of the pulse following the trigger. The 2D histogram of the tail fraction and the total energy deposition for a single detector over the course of one of the data runs is shown in Figure 5. For each energy bin in each detector, a Gaussian profile was fit to the central tail/total ratio peak to produce a cut at 3σ for each energy bin in each detector to reject events as pile-up. The resulting cut region on the PSD parameter for an example detector is also shown in Figure 5.

Rejecting events identified as pile-up, however, introduces an effective deadtime to the measurement (since no counts are accepted in an integration window with pile-up). Since the presence of material in the beam significantly affects the pile-up rate, the pile-up rejected spectra on their own are not representative of the actual transmitted flux compared to the open beam. For the open beam, approximately 70% of recorded energy depositions were rejected due to pile-up (after correction for the Gaussian cut boundaries). Since each of these pile-up events represents at least two individual photons, use of the uncorrected pile-up rejected spectrum would result in underestimating the true flux by >500%, and would introduce similarly large errors in the transmission ratio. Due to the long integration window, pile-up deadtime dominated the total effective deadtime. Additional data acquisition and processing time added $\ll 1\%$ to the effective deadtime, and was not included as a significant correction.

To account for this, a pile-up correction was devised. Given that individual true events are independent, the true energy spectrum of counts that are recorded in the pile-up portion of the data matches the energy spectrum of the counts that occurred without pile-up, up to secondary effects such as small additional energy pile-up and associated trigger bias. Thus the desired correction may be approximated as a scaling factor that is applied to

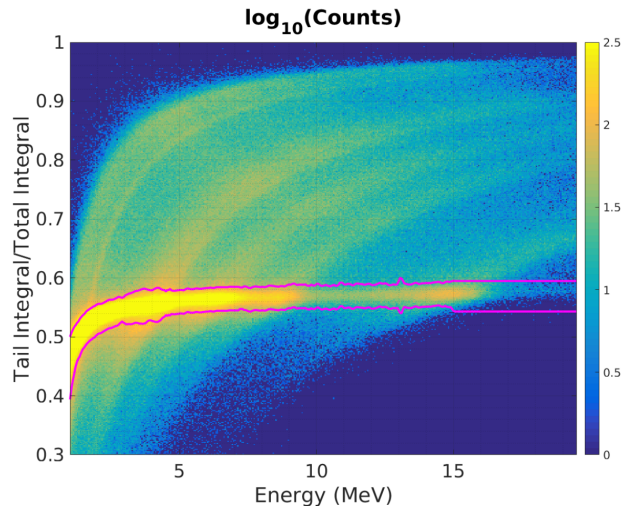


FIG. 5. Two-dimensional “tail-over-total” PSD histogram (\log_{10} counts) for the raw spectrum of the open beam. The bright band at a ratio of ~ 0.55 represents windows with a single detected photon. The curved bands away from the main band show pile-up events, in which additional energy is added to the common monoenergetic depositions (above the main band) or in which a monoenergetic event occurs close enough to the end of a trigger window for its tail to cause another trigger (below the main band). The region between the magenta lines indicates the pile-up cut region.

the pile-up rejected (“clean”) spectrum. Since the true rate of individual events r is unknown, and the resolving time of the detector τ may also be unknown, it is most useful to express the standard formulation of pile-up³⁷ as a function of the fraction f of total counts captured in the pile-up rejected spectrum. For the long, fixed ADC integration window used in this experiment, the deadtime was of a non-paralyzable nature. As derived in Appendix B, the true spectrum N may thus be reconstructed from the pile-up rejected spectrum N_C as:

$$N = N_C \left(\frac{1 - \ln f}{f} \right). \quad (3)$$

This correction was applied to each time/position step of the image scans to account for variation in the pile-up rate over the course of the experiments.

B. Simulation Model

A complete simulation model of the experiment was constructed, including all relevant aspects of the experiment, to compute simulated transmission spectra for a wide variety of materials that could be directly compared to the data. By using such a model, the need for empirical calibration of the system with sample data from many materials was avoided. The simulation model was constructed using the Geant4 toolkit²⁵, and included all important physical materials present in the experiment

(the neutron shield in the beamline, the collimators, the detectors, etc.) at positions surveyed during data taking. Photons originating at the boron target were propagated through the geometry (including any simulated cargo material) to the model detectors, which included simulated responses — resolution, efficiency, etc. — modeled according to dedicated empirical tests.

The simulated beam was generated by simulating the five major monoenergetic beam components shown in Figure 2 (1.7, 4.4, 6.7, 8.9, and 15.1 MeV) for fixed geometries, and determining their relative contribution to the beam using an empirical fit to data taken in dedicated experiments. The resulting simulated spectra for each monoenergetic contribution were convolved with the simulated detector response, and then the relative strength of each contribution was fit so as to best match the corresponding data. The results of the fit for the open beam is shown in Figure 6. Note that while the analysis depends only on relative transmission, this beam model accounts for the contributions in 4.4 MeV region due to down-scatter and incomplete energy deposition in the detectors from higher energy photons to increase the accuracy of the analysis. Figure 7 shows the simulation prediction for the transmission spectrum for a copper sample of $\rho_A \approx 49$ g/cm². This prediction is based on propagation of the reconstructed open beam (Figure 6) through a simulated material sample using Geant4. These predicted spectra were compared to the data spectra to reconstruct materials, as described in Section III C.

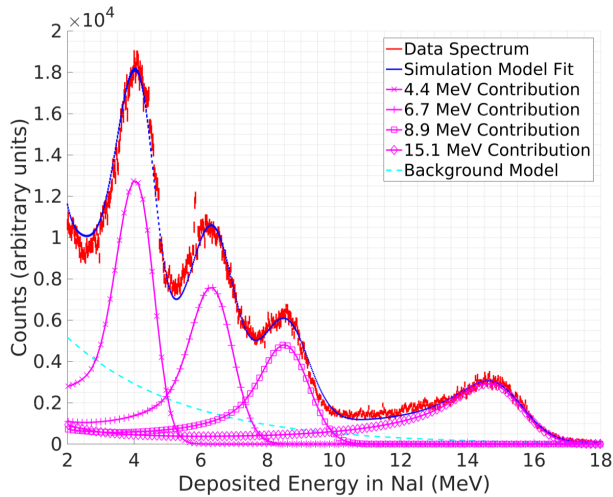


FIG. 6. The simulation spectrum fit to an open beam data sample taken using a single NaI (TI) detector (color online). The individual simulated contribution magnitudes, detector model parameters, and background model were fit to best match the data for each sample.

Approximately 5000 simulated transmission experiments were generated to create a library of expected detected spectra over the complete two-dimensional space of $Z = 4$ –92 and $\rho_A = 20$ –250 g/cm², in addition to the open beam configuration. As described in Section III C,

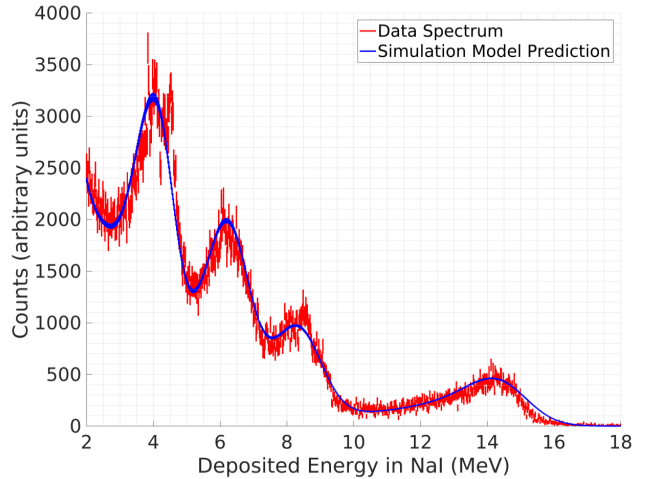


FIG. 7. Comparison of the data spectrum from a pixel in the copper region of the 2000 s scan to the simulation prediction based on the fit to the open beam spectrum of Figure 6, given knowledge of the material in the beam at the time.

this simulation library was compared to the transmission data to estimate the areal density and effective Z of each pixel in a scan.

C. Radiographic Reconstruction

With data and simulation spectra prepared, the transmission ratios for each data and simulation spectrum were computed in the regions of the 4.4 MeV and 15.1 MeV peaks. For each spectrum (with the simulation and data treated in the same manner), the counts between 2.8 MeV and 5.0 MeV (so as to encompass the full deposition and escape peaks of the 4.4 MeV photons) were integrated to compute N_4 , while all counts above 10.1 MeV were integrated to produce N_{15} (since essentially all counts above this energy were due to incomplete energy depositions of 15.1 MeV photons). The simulation was run with no mock cargo to produce an open beam spectrum for the transmission calculation, while the data runs used the open beam spectra collected during the first and last portions of the run (normalized to the integrated current of one pixel). The transmission ratios in each energy bin E were defined as

$$R_E = \frac{N_E}{N_{E,\text{open}}}, \quad (4)$$

where the $N_{E,\text{open}}$ are the integrated counts for the appropriate open beam spectra, after applying the corrections discussed in Section III A.

With the transmission ratios for the data and simulation spectra in the regions of interest determined, a figure of merit F was constructed to determine the simulated combination of Z and ρ_A that best matched the

data spectrum. The quantity was constructed using ratios of the transmission ratios (Equation 4) in the 4.4 and 15.1 MeV regions to construct a quantity robust against a number of systematic uncertainties. For each pixel, the data spectrum was compared to each element of the simulated material library with effective Z and ρ_A according to

$$F(Z, \rho_A) = \left(\frac{R_{15, \text{data}}}{R_{15, \text{sim}}(Z, \rho_A)} - 1 \right)^2 + \left(\frac{R_{4, \text{data}}/R_{15, \text{data}}}{R_{4, \text{sim}}(Z, \rho_A)/R_{15, \text{sim}}(Z, \rho_A)} - 1 \right)^2. \quad (5)$$

This metric was motivated by the fact that the signal in the 15.1 MeV region was very clean due to the absence of high energy backgrounds in the data and the fact that the ratio-of-ratios between the 4.4 and 15.1 MeV regions provides strong material discrimination while canceling certain systematic uncertainties. The values of Z and ρ_A corresponding to the minimum of F were assigned as the reconstructed values for each pixel, noting that a perfect match between the measured and simulated transmission results in $F = 0$. Figure 8 shows examples of the reconstruction for a low- Z material (Al) and a high- Z material (W).

IV. RESULTS

To produce images of the mock cargo in effective Z and areal density, the data spectra were grouped into 1 cm pixels along the scan length. For each pixel, the radiographic analysis described in Section III was applied to produce the images in effective Z and areal density ρ_A . Figure 9 shows the results for the 7400 s scan. In addition to the pixel-by-pixel estimate, regions were defined according to the boxes shown in the reconstruction images to quantitatively evaluate the performance of the analysis for each material. For each region, the average reconstructed Z and ρ_A were computed for comparison to the known true values. These results are summarized in Tables II and III for the 7400 s and 2000 s scans, respectively. The standard deviation of each estimated pixel value was used as a measure of the uncertainty on the values reconstructed for each individual pixel, which were then used to compute the uncertainties on the overall mean reconstructed values.

The reconstructed values are very close to the true values in both of the imaging tests, showing the robustness of the system and analysis to environmental drift effects (e.g., temperature changes) and the statistics of the data (the 7400 s run included approximately 4 times as many counts in the transmission spectra per pixel as the 2000 s run). It should also be noted that while the absolute values are close to the true values, there are residual statistically significant differences. This indicates that further improvements to the reconstruction algorithms or control of systematic uncertainties are possible, and thus

should be part of future work. Despite this limitation, the specificity of the monoenergetic beam transmission provides effective atomic number identification with specificity of ± 3 in Z and thus permits separation of different high- Z materials, which is typically not possible in existing radiography systems. For example, the tungsten and lead samples are well separated in reconstructed atomic number, while the areal density reconstruction is also accurate for each material to within a few g/cm². This suggests that pure special nuclear materials ($Z \geq 92$) could be separated from benign high- Z materials such as lead and tungsten, which would be invaluable for reducing false alarms in a system designed to detect nuclear smuggling.

The results for the mixed material uranium rods merit further discussion. Due to the fact that the rods consist of aluminum and uranium, and additionally because they are not uniform in areal density as presented to the beam, evaluation of the reconstruction of the material parameters for the rods is not as straightforward as for the pure materials. Appendix A details rough estimates of the expected effective Z and areal density for the arrangement of the rods, up to the limited information available about the exact composition of the rods. Due to the fact that the 1 cm pixel size in Figure 9 obscures the structures predicted by the results in Figure 12, it is useful to consider 1 mm pixels for the uranium rod sample despite the reduction in statistics. Figure 10 shows the reconstructed Z and ρ_A for the rods with 1 mm pixels. While the areal density is slightly overestimated in the 1 mm pixels (due to low statistics), the images in Figure 10 clearly show the structure of the rod arrangement (Figure 11), and show that extra spacing between the rightmost rods in combination with the uncertainty on the rod composition is likely responsible for the discrepancies between the reconstructed Z and ρ_A values and the estimates from Appendix A. This mixed material example demonstrates the limitations of 2D radiographic imaging to determine the material composition of cargo, but with sufficient position resolution the presence of high- Z material is still clearly evident.

V. CONCLUSIONS AND FUTURE WORK

The results presented here establish the use of multiple monoenergetic gamma ray radiography (MMGR) to image materials in both their effective atomic number and areal density. Most notably, the technique distinguishes pure materials even at high- Z (e.g., separating Pb and W or Pb and U), a critical requirement of any system designed to detect SNM and differentiate it from benign high- Z materials, which could otherwise result in false positive detections. The specific information transmitted by the monochromatic beam, combined with high resolution detectors to clearly identify directly transmitted photons, provides the capability to identify materials while minimizing the radiation dose delivered to the

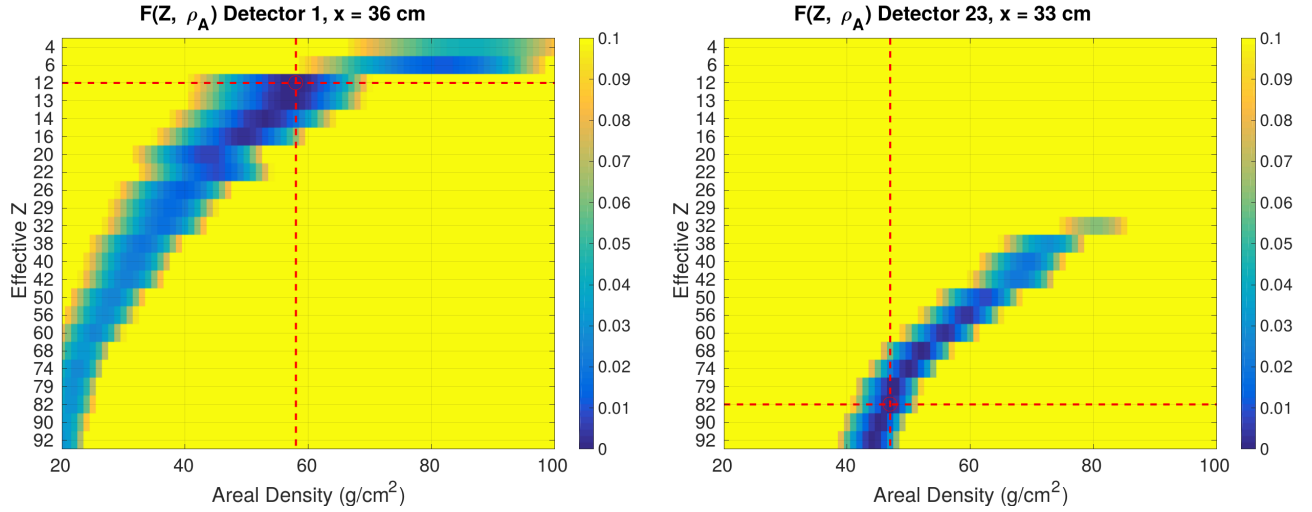


FIG. 8. Two examples of the data/simulation comparison metric F (Equation 5) as a function of Z and ρ_A over the simulation library. Examples from the aluminum (left) and tungsten (right) regions of the 7400 s test are shown. The crossing dashed lines indicate the minimum of F in each plot, showing the reconstructed Z and ρ_A values.

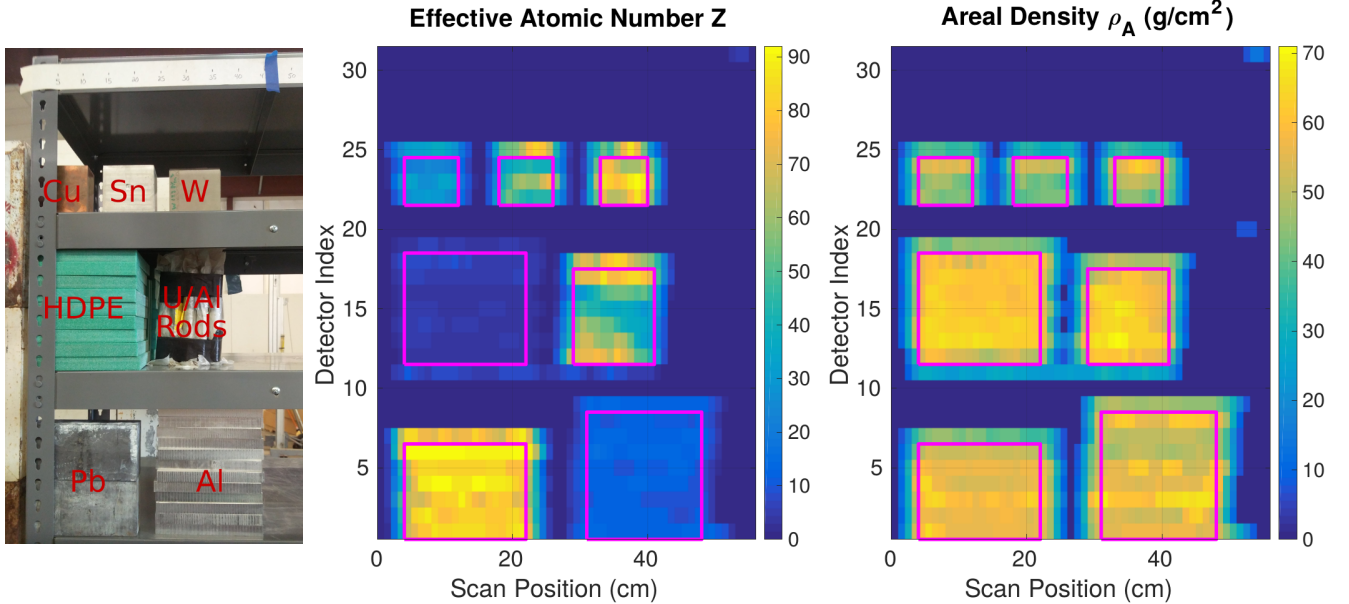


FIG. 9. Images of the mock cargo in reconstructed effective Z and areal density for the 7400 s test (~ 1.3 mC integrated deuteron beam current on target per cm of the scan). The magenta boxes show the regions used to define each material sample for the computation of the values in Table II.

cargo.

The results for the natural uranium rods demonstrate the fundamental limitations of this technique, and indeed radiography of any kind, as a method for detecting SNM. The several mm of aluminum cladding significantly reduces the effective Z of the configuration, somewhat masking the presence of the uranium. With sufficient position resolution, however, the presence of very high- Z (>80) material can be flagged for this configuration. This suggests that monoenergetic gamma ray radiography may be paired with a secondary technique

(such as a system designed to detect induced photofission neutrons^{6,22}) to disambiguate such situations. Additionally, future work will explore the resolving power of radiography using multiple projections for mixed material configurations.

A concern that has been raised regarding high energy gamma radiography techniques is the resulting radiological activation of inspected materials. Photons at 15.1 MeV have enough energy to induce (γ, n) photodisintegration reactions in many elements, and may indirectly become a source of neutrons. The capture of

Material	Actual Z	Reconstructed Z	Single Pixel Unc.	Actual ρ_A (g/cm ²)	Reconstructed ρ_A (g/cm ²)	Single Pixel Unc. (g/cm ²)
Borated HDPE	~ 5.2	4.7 ± 0.1	(1.4)	46.2	60.5 ± 0.5	(5.3)
Aluminum (Al)	13	12.0 ± 0.2	(2.1)	54.7	55.8 ± 0.6	(7.2)
Copper (Cu)	29	27.5 ± 1.1	(5.6)	48.8	48.0 ± 1.2	(6.0)
Tin (Sn)	50	49.1 ± 2.9	(14.0)	49.3	45.0 ± 1.3	(6.2)
Tungsten (W)	74	75.3 ± 3.3	(15.1)	49.4	50.0 ± 1.7	(8.0)
Lead (Pb)	82	83.2 ± 0.9	(9.3)	57.7	56.8 ± 0.4	(4.5)
Uranium rods	~ 65	55.5 ± 2.3	(19.3)	~ 55	61.3 ± 0.8	(7.0)

TABLE II. Reconstructed effective Z and areal density values for the mock cargo materials for the 7400 s test (~ 1.3 mC integrated deuteron beam current on target per cm of the scan). Quoted uncertainty after the “ \pm ” represents the uncertainty on the average over the material region, while the single pixel uncertainty is the standard deviation of the single pixel ($1\text{ cm} \times 1$ detector) estimates over the region. See Figure 9 for the definition of each sample region.

Material	Actual Z	Reconstructed Z	Single Pixel Unc.	Actual ρ_A (g/cm ²)	Reconstructed ρ_A (g/cm ²)	Single Pixel Unc. (g/cm ²)
Borated HDPE	~ 5.2	5.9 ± 0.2	(2.4)	46.2	61.7 ± 0.7	(7.9)
Aluminum (Al)	13	12.4 ± 0.4	(4.6)	54.7	53.8 ± 0.9	(10.0)
Copper (Cu)	29	28.2 ± 1.3	(6.6)	48.8	47.8 ± 1.2	(5.9)
Tin (Sn)	50	49.7 ± 3.3	(16.1)	49.3	46.5 ± 1.5	(7.1)
Tungsten (W)	74	75.8 ± 3.8	(18.4)	49.4	47.7 ± 1.8	(8.9)
Lead (Pb)	82	80.9 ± 1.7	(18.1)	57.7	65.1 ± 2.2	(23.4)
Uranium rods	~ 65	59.4 ± 2.5	(20.5)	~ 55	63.2 ± 2.0	(16.5)

TABLE III. Reconstructed effective Z and areal density values for the mock cargo materials for the 2000 s test (~ 0.33 mC integrated deuteron beam current on target per cm of the scan). Quoted uncertainty after the “ \pm ” represents the uncertainty on the average over the material region, while the single pixel uncertainty is the standard deviation of the single pixel ($1\text{ cm} \times 1$ detector) estimates over the region.

these secondary neutrons can transmute stable isotopes into metastable ones and induce long-lived radioactivity in the inspected materials. Calculations show, however, that the exposure to the neutrons produced by the above reaction amounts to just one hour of exposure to cosmogenic neutrons from the natural background, and as such any contributions to induced radioactivity is negligible when compared naturally occurring activation. This calculation is detailed in Appendix C.

The experimental setup used here would require significant modifications for deployment as a cargo scanning system, several of which are the subject of ongoing work. As discussed at the end of Section II, the scan times of several thousand seconds used in this work would be reduced to $\lesssim 2$ minutes by operating at mA-scale current. The results presented here demonstrate the ability of a radiography system to function in counting mode at such currents using the pile-up correction technique detailed in Section III A 4. In such a system, another technique would likely need to be devised to account for the background subtraction conducted here using timing information. Additionally, the use of alternate nuclear reactions such as $^{12}\text{C}(p, p'\gamma)^{12}\text{C}$ and $^{16}\text{O}(p, p'\gamma)^{16}\text{O}$, which produce monoenergetic gamma rays between 4.4 and 8.9 MeV, would open a variety of options for different accelerators and significantly reduce the neutrons that are present from other processes in a system using $^{11}\text{B}(\text{d}, n\gamma)^{12}\text{C}$.

Work is ongoing to establish the applicability of the techniques for precision material identification described in this paper using the lower energy photons available from such reactions.

ACKNOWLEDGEMENTS

This work is supported in part by the U.S. Department of Homeland Security Domestic Nuclear Detection Office under a competitively awarded collaborative research ARI-LA Award, ECCS-1348328 and is part of a collaboration between the Massachusetts Institute of Technology, Georgia Institute of Technology, University of Michigan, and Pennsylvania State University. This support does not constitute an express or implied endorsement on the part of the United States Government. The authors are grateful to Richard C. Lanza, who developed some of the initial ideas behind this work, for his support, encouragement, and valuable advice. BSH gratefully acknowledges the support of the Stanton Foundation Nuclear Security Fellowship. The authors wish to thank the MIT-Bates Research and Engineering Center staff for their invaluable contributions to the construction and operation of the experiment; in particular Peter Binns, Hamid Moazeni, and Ernest Ihloff. They thank Taylor Sims for his work on the experiment during

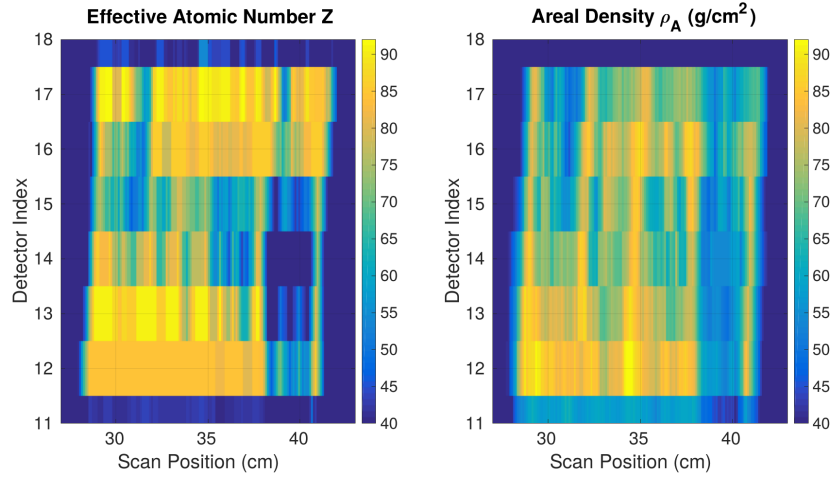


FIG. 10. Images of the uranium rods in reconstructed effective Z and areal density for the 7400 s test (~ 1.3 mC integrated deuteron beam current on target per cm of the scan) with 1 mm wide pixels.

data taking. Additionally, they thank Igor Jovanovic and Jayson Vavrek for valuable comments on the manuscript.

Appendix A: Calculation of the Uranium Rod Effective Z and Areal Density

As described in Section II D, the mock cargo objects for the imaging demonstration results in this paper consisted of approximately uniform density pure elemental materials except for the natural uranium rods. These rods, used on loan from the MIT Nuclear Reactor Laboratory, consisted of cylinders of natural uranium metal clad with 0.3 cm of aluminum (for a total diameter of 2.75 cm). For the imaging test, 10 of these rods were arranged in two rows of five as shown in Figure 11.

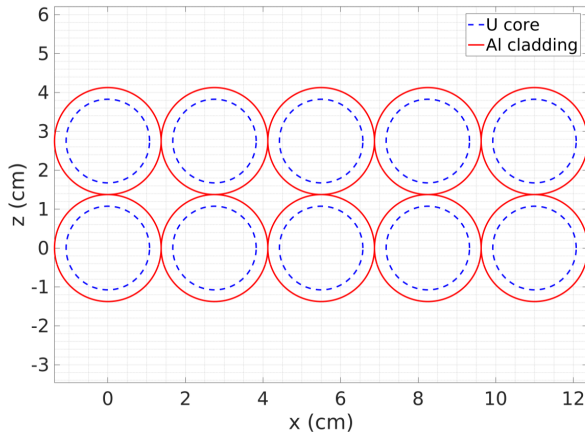


FIG. 11. Arrangement of the 10 natural uranium rods used in the imaging test, viewed from above. The beam was incident in the $+\hat{z}$ direction.

Due to the fact that there was no means of verifying the internal composition of the rods, the following calculations assume that the uranium metal inside the cladding was of uniform density 19.3 g/cm^3 . Given this assumption, it is possible to compute the areal density along the beam path across the arrangement of the rods. To compare to the imaging results, however, the averaging effect of the finite collimator width must be considered. At the position of the mock cargo, the collimation produced a beam width of approximately 2.4 cm. A sliding average over this width was applied to the exact calculation of the areal density to produce the expected reconstructed areal density, shown in Figure 12.

Computation of the expected effective Z requires consideration of the nature of the beam and physical processes that contribute to the attenuation of the beam for the aluminum and uranium combinations across the arrangement. To estimate this value, the photon mass attenuation coefficients ($\frac{\mu}{\rho}$) for the uranium and aluminum combinations across the configuration were estimated as functions of energy according to

$$\frac{\mu}{\rho} = w_U \cdot \left(\frac{\mu}{\rho} \right)_U + (1 - w_U) \cdot \left(\frac{\mu}{\rho} \right)_{Al}, \quad (\text{A1})$$

where w_U is the uranium mass fraction at a given position, as computed above, and the attenuation coefficient values for the individual elements provided by the NIST x-ray mass attenuation coefficient database³⁸. For each position in the configuration, the pure element with attenuation coefficient values at 4.4 MeV and 15.1 MeV best matching the rod attenuation coefficients as computed by Equation A1 was used as an estimate of the effective value of Z at that position. The results of this estimate, averaged over the beam illumination width, are also shown in Figure 12.

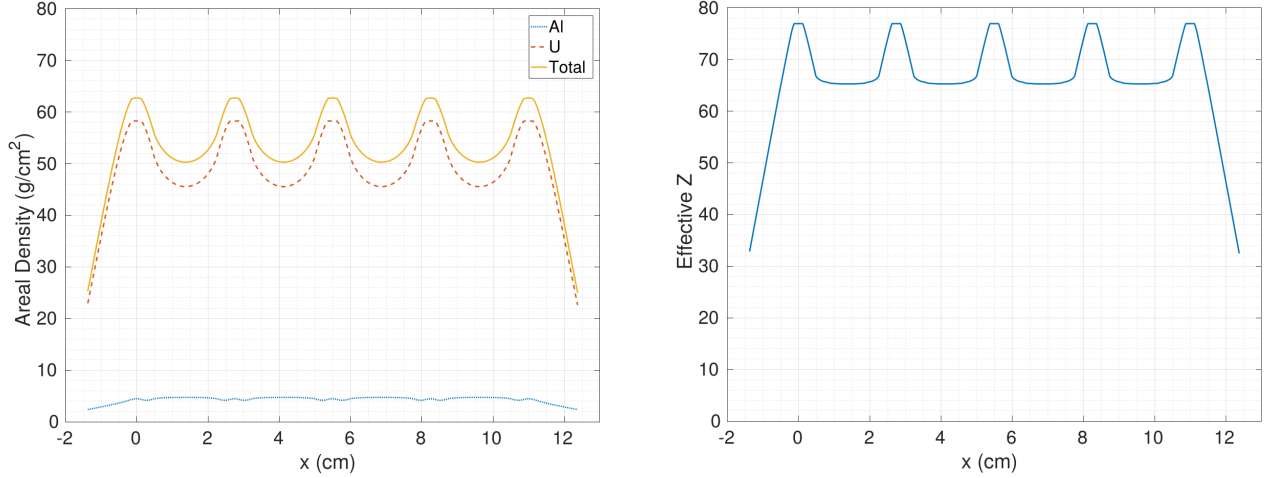


FIG. 12. Expected reconstructed areal density (left) and effective Z (right) of the uranium rod arrangement along the beam path, accounting for the loss of resolution due to the 2.38 cm width of the beam.

Appendix B: Calculation of the Pile-Up Correction Factor

In this appendix, the scaling factor that must be applied to a pile-up rejected (“clean”) spectrum with counts N_C is computed for both paralyzable and non-paralyzable deadtime scenarios. Since the true rate of individual events r is unknown, and the resolving time of the detector τ may also be unknown, it is most useful to express the correction as a function of the fraction of total counts captured in the pile-up rejected spectrum f (i.e., the “clean” fraction of events).

To compute the correction, let N_{rec} be the total number of recorded counts (including pile-up rejected counts), N_c be the number of counts recorded cleanly without pile-up, and N_{pu} be the number of counts in the pile-up portion of the spectrum (or the number of rejected counts). That is, $N_{\text{rec}} = N_c + N_{\text{pu}}$. The number of true counts N may then be expressed as

$$N = N_c + N_{\text{pu}} \cdot \bar{n}, \quad (\text{B1})$$

where \bar{n} is the mean number of true counts per pile-up count. Since the clean spectrum represents the correct shape of the true spectrum, it is useful to express Equation B1 as a scaling of the number of clean counts as the fraction $f = \frac{N_c}{N_{\text{rec}}}$ of the total recorded counts that they represent:

$$N = N_c \left(1 + \frac{N_{\text{rec}} - N_c}{N_c} \cdot \bar{n} \right) = N_c \left(1 + \frac{1-f}{f} \cdot \bar{n} \right). \quad (\text{B2})$$

The true spectrum may then be recovered by scaling the extracted clean spectrum, given the mean number of true counts per pile-up count \bar{n} . Let $P(j)$ be the probability that given a single true event, j additional events are recorded as piled-up with the original event (i.e., $j =$

0 represents a cleanly recorded event). Then the mean number of counts per piled-up count is:

$$\bar{n} = \frac{1}{\sum_{j=1}^{\infty} P(j)} \sum_{j=1}^{\infty} (j+1) P(j) = \frac{1}{1-f} \sum_{j=1}^{\infty} (j+1) P(j), \quad (\text{B3})$$

since the term in the denominator is simply the probability that the original count accumulates at least one additional count when recorded.

The following sections compute \bar{n} as a function of f for the cases of non-paralyzable and paralyzable detector and data acquisition systems, re-expressing the standard results for pile-up rates³⁷ to eliminate need for knowledge of the true detector rates and resolving times.

1. Non-Paralyzable Case

For a non-paralyzable detector and data acquisition system exposed to a true rate of incident events r with an integration time of τ per recorded event, the probability $P(j)$ of j true events following a given event trigger within the same trigger window is governed by the Poisson distribution³⁷:

$$P(j) = \frac{(r\tau)^j}{j!} e^{-r\tau}. \quad (\text{B4})$$

Combining Equations B3 and B4 for the non-paralyzable case yields

$$\bar{n}_{\text{NP}} = \frac{e^{-r\tau}}{1-f} \sum_{j=1}^{\infty} (j+1) \frac{(r\tau)^j}{j!}. \quad (\text{B5})$$

Noting that $\exp(x) = \sum_{j=0}^{\infty} x^j/j!$, the sums reduce to

$$\bar{n}_{\text{NP}} = \frac{1}{1-f} (1 - e^{-r\tau} + r\tau). \quad (\text{B6})$$

As noted, it is most useful to recast the expression as a function of the fraction of the total counts in the pile-up rejected spectrum $f = P(0) = e^{-r\tau}$, to yield

$$\bar{n}_{\text{NP}} = 1 - \frac{\ln f}{1 - f}. \quad (\text{B7})$$

Note that \bar{n}_{NP} monotonically increases with the piled-up fraction $(1 - f)$ and $\lim_{f \rightarrow 1} \bar{n}_{\text{NP}} = 2$, i.e., piled-up events contain a negligible fraction of multiple pile-up ($j > 1$) as the pile-up rate goes to zero.

2. Extending Case

In the paralyzable case, the arrival of each new true event resets the integration time τ per event, leading to a greater probability of accumulating $j > 1$ piled-up true events along with the event that initialized the trigger. The probability of j events piling-up with a given single event which initializes a trigger for the paralyzable system case is³⁷

$$P(j) = e^{-r\tau} (1 - e^{-r\tau})^j. \quad (\text{B8})$$

Note that, as in the non-paralyzable case, $f = P(0) = e^{-r\tau}$. Combining Equations B3 and B8 yields

$$\bar{n}_{\text{P}} = \frac{f}{1 - f} \sum_{j=1}^{\infty} (j + 1) (1 - f)^j. \quad (\text{B9})$$

Since $0 \leq f \leq 1$, the sum is an arithmetico-geometric series:

$$\bar{n}_{\text{P}} = 1 + \frac{1}{f}. \quad (\text{B10})$$

This quantity also approaches $\bar{n} = 2$ for $f \rightarrow 1$ like Equation B7, but increases much more rapidly as f goes to zero, as expected for the extended integration window.

Appendix C: Neutrons from the (γ, n) reactions

The 15.1 MeV photons in the presented system have energies well above the photodisintegration thresholds for a number of common materials, and thus can produce neutrons via the $X(\gamma, n)Y$ reaction. The resulting radiological activation of inspected materials resulting from transmutation of nuclei into unstable isotopes as these neutrons are captured has been a commonly cited concern regarding the use of high energy gamma rays for cargo inspection³⁹. To understand the scale of this effect, it is useful to estimate the production rate for these neutrons and compare it to the rate of exposure to cosmogenic neutrons.

As an example, consider the case of a plate of steel 2.4 m tall, undergoing a scan at the speed of 40 cm/s with

15.1 MeV photons. The rate of neutron production in the steel is

$$N = \frac{\sigma N_A}{A} \phi_0 \frac{1}{\mu} [1 - e^{-\mu \rho D}], \quad (\text{C1})$$

where N is the neutron production rate, σ is the (γ, n) total cross section, $N_A = 6.022 \times 10^{23}$ is Avogadro's number, A is the atomic weight of the target material, ϕ_0 is the incident photon rate, μ is the mass attenuation cross section, ρ is the density, and D is the thickness of the material.

For a realistic cargo scanning system using the $^{11}\text{B}(\text{d}, \text{n}\gamma)^{12}\text{C}$ reaction with 1 mA of deuteron current, $\phi_0 \approx 2 \times 10^{10} \text{ mA}^{-1} \text{ s}^{-1}$ ⁽²¹⁾, assuming a collimation width of 3 mm at a distance 1 m from the target. Taking $D \gg 1/\mu\rho$, i.e. a thick slab, $\sigma = 40 \text{ mb}$ ⁽⁴⁰⁾, and $\mu = 0.031 \text{ cm}^2/\text{g}$ ⁽³¹⁾, the neutron production rate would be $N = 4.2 \times 10^5 \text{ s}^{-1}$. For a comparison, the cosmogenic neutron rate is estimated by Gordon *et al.*⁴¹ is approximately $0.0134 \text{ cm}^{-2} \text{ s}^{-1}$, which includes contributions from thermal neutrons in addition to the fast neutrons of interest for this comparison. Integrating over the volume of the plate described above, the cosmogenic neutron exposure rate is $N_{\text{cosm.}} \approx 130 \text{ s}^{-1}$. The neutron production by (γ, n) reactions in the steel plate is approximately 3300 times higher than the exposure to cosmogenic neutrons, which corresponds to only ~ 1 hour of effective additional exposure to natural neutron background. As such, the exposure to the high energy gamma rays in a single scan has a negligible effect on the additional buildup of transmuted elements and activation of the material.

REFERENCES

- ¹C. Meade and R. C. Molander, *Considering the Effects of a Catastrophic Terrorist Attack* (RAND Corporation, Santa Monica, CA, 2006).
- ²C. C. Abt, "The economic impact of nuclear terrorist attacks on freight transport systems in an age of seaport vulnerability," Abt Associates Inc. Exective Summary (2003).
- ³R. Kouzes *et al.*, *Radiation Detection and Interdiction at U.S. Borders* (Oxford University Press, 2011) p. 23.
- ⁴Congressional Budget Office, "Scanning and Imaging Shipping Containers Overseas: Costs and Alternatives," Report to the Congress of the United States (2016).
- ⁵World Customs Organization, "Guidelines for the Procurement and Deployment of Scanning/NII Equipment," (2015).
- ⁶A. Danagoulian *et al.*, in *Proceedings of 2010 IEEE International Conference on Technologies for Homeland Security (HST)* (IEEE, 2010) pp. 379–384.
- ⁷R. Ledoux and W. Bertozzi, "Methods and systems for determining the average atomic number and mass of materials," (2007), US Patent 7,286,638.

- ⁸W. Bertozzi and R. J. Ledoux, Nucl. Instrum. Meth. **B 241**, 820 (2005).
- ⁹M. Mayer, J. Nattress, and I. Jovanovic, Applied Physics Letters **108**, 264102 (2016).
- ¹⁰R. C. Runkle, D. L. Chichester, and S. J. Thompson, Nucl. Instrum. Meth. **A 663**, 75 (2012).
- ¹¹N. King *et al.*, Nucl. Instrum. Meth. **A 424**, 84 (1999).
- ¹²L. J. Schultz *et al.*, Nucl. Instrum. Meth. **A 519**, 687 (2004).
- ¹³C. Morris, C. Alexander, J. Bacon, K. Borozdin, D. Clark, R. Chartrand, C. Espinoza, A. Fraser, M. Galassi, J. Green, *et al.*, Science & Global Security **16**, 37 (2008).
- ¹⁴K. N. Borozdin, G. E. Hogan, C. Morris, W. C. Friedrichsky, A. Saunders, L. J. Schultz, and M. E. Teasdale, Nature **422**, 277 (2003).
- ¹⁵J. Rahon *et al.*, Nucl. Instrum. Meth. **A 820**, 141 (2016).
- ¹⁶B. Sowerby and J. Tickner, Nucl. Instrum. Meth. **A 580**, 799 (2007).
- ¹⁷N. G. Cutmore, Y. Liu, and J. R. Tickner, in *Technologies for Homeland Security (HST), 2010 IEEE International Conference on* (IEEE, 2010) pp. 330–336.
- ¹⁸G. Chen, G. Bennett, and D. Perticone, Nucl. Instrum. Meth. **A 261**, 356 (2007).
- ¹⁹A. J. Gilbert, B. S. McDonald, S. M. Robinson, K. D. Jarman, T. A. White, and M. R. Deinert, Journal of Applied Physics **115**, 154901 (2014), <http://dx.doi.org/10.1063/1.4870043>.
- ²⁰B. E. O'Day, *A Novel Low-dose Approach to Active Detection of Shielded High-Z Material*, Ph.D. thesis, Massachusetts Institute of Technology (2015).
- ²¹B. E. O'Day *et al.*, Nucl. Instrum. Meth. **A 506**, 68 (2016).
- ²²P. B. Rose *et al.*, Sci. Rep. **6** (2016).
- ²³W. Leo, *Techniques for Nuclear and Particle Physics Experiments* (Springer-Verlag Berlin Heidelberg, 1994).
- ²⁴Q. Li *et al.*, Journal of Tsinghua University (Science and Technology) **8**, 007 (2008).
- ²⁵S. Agostinelli *et al.* (GEANT4), Nucl. Instrum. Meth. **A 506**, 250 (2003).
- ²⁶K. W. Cooper *et al.*, Nucl. Instrum. Meth. **B 305**, 45 (2013).
- ²⁷C. Class, J. Price, and J. Risser, Nuclear Physics **71**, 433 (1965).
- ²⁸“NaI(Tl) and Polyscin[®] NaI(Tl) Sodium Iodide,” <https://www.crystals.saint-gobain.com/products/nai-sodium-iodide> (Accessed: January 10, 2018).
- ²⁹“V1725,” <http://www.caen.it/csite/CaenProd.jsp?parent=11&idmod=952> (Accessed: January 10, 2018).
- ³⁰Z. S. Hartwig, Nucl. Instrum. Meth. **A 815**, 42 (2016).
- ³¹M. J. Berger *et al.*, “XCOM: Photon Cross Section Database (version 1.5),” <http://physics.nist.gov/xcom> (Accessed: January 3, 2018) (2010).
- ³²J. Stevenson *et al.*, Nucl. Instrum. Meth. **A 652**, 124 (2011), symposium on Radiation Measurements and Applications (SORMA) XII 2010.
- ³³N. W. Tanner, The Philosophical Magazine: A Journal of Theoretical Experimental and Applied Physics **1**, 47 (1956), <https://doi.org/10.1080/14786435608238075>.
- ³⁴J. Kelley, J. Purcell, and C. Sheu, Nuclear Physics A **968**, 71 (2017).
- ³⁵J. Kelley, E. Kwan, J. Purcell, C. Sheu, and H. Weller, Nuclear Physics A **880**, 88 (2012).
- ³⁶J. Adams and G. White, Nucl. Instrum. Meth. **156**, 459 (1978).
- ³⁷G. F. Knoll, *Radiation Detection and Measurement* (Wiley, New York, NY, 2000) pp. 636 – 643.
- ³⁸J. H. Hubbell and S. M. Seltzer, “Tables of X-Ray Mass Attenuation Coefficients and Mass Energy-Absorption Coefficients (version 1.4),” <https://www.nist.gov/pml/x-ray-mass-attenuation-coefficients> (Accessed: January 3, 2018) (2004).
- ³⁹J. I. Katz, G. S. Blanpied, K. N. Borozdin, and C. Morris, Science & Global Security **15**, 49 (2007), <https://doi.org/10.1080/08929880600993030>.
- ⁴⁰M. Chadwick *et al.*, Nuclear Data Sheets **112**, 2887 (2011), Special Issue on ENDF/B-VII.1 Library.
- ⁴¹M. Gordon *et al.*, IEEE Transactions on Nuclear Science **51**, 3427 (2004).